

REVERBERATION MAPPING OF THE SEYFERT 1 GALAXY NGC 7469

B. M. PETERSON^{1,2}, C. J. GRIER^{1,3}, KEITH HORNE⁴, R. W. POGGE^{1,2}, M. C. BENTZ⁵, G. DE ROSA^{1,6},
 K. D. DENNEY^{1,22}, PAUL MARTINI^{1,2}, S. G. SERGEEV⁷, S. KASPI^{8,9}, T. MINEZAKI¹⁰, Y. ZU^{1,11}, C. S. KOCHANÉK^{1,2},
 R. J. SIVERD¹², B. SHAPPEE¹, C. ARAYA SALVO¹, T. G. BEATTY^{1,3}, J. C. BIRD^{1,12}, D. J. BORD¹³, G. A. BORMAN⁷,
 X. CHE¹⁴, C.-T. CHEN¹⁵, S. A. COHEN¹⁵, M. DIETRICH^{16,17}, V. T. DOROSHENKO^{7,18}, T. DRAKE⁵, YU. S. EFIMOV^{7,23},
 N. FREE¹⁶, I. GINSBURG¹⁵, C. B. HENDERSON¹, A. L. KING¹⁴, S. KOSHIDA^{10,19}, K. MOGREN¹, M. MOLINA^{1,3},
 A. M. MOSQUERA¹, K. MOTOHARA¹⁰, S. V. NAZAROV⁷, D. N. OKHMAT⁷, O. PEJCHA^{1,20,24}, S. RAFTER⁹,
 J. C. SHIELDS¹⁶, D. M. SKOWRON^{1,21}, J. SKOWRON^{1,21},
 M. VALLURI¹⁴, J. L. VAN SADERS¹, AND Y. YOSHII¹⁰

¹ Department of Astronomy, The Ohio State University, 140 West 18th Avenue, Columbus, OH 43210, USA; peterston.12@osu.edu

² Center for Cosmology and AstroParticle Physics, The Ohio State University, 191 West Woodruff Avenue, Columbus, OH 43210, USA

³ Department of Astronomy and Astrophysics, Eberly College of Science, Penn State University,
 525 Davey Laboratory, University Park, PA 16802, USA

⁴ SUPA Physics and Astronomy, University of St. Andrews, Fife KY16 9SS, UK

⁵ Department of Physics and Astronomy, Georgia State University, Astronomy Offices, 25 Park Place, Suite 605, Atlanta, GA 30303, USA

⁶ Space Telescope Science Institute, 3700 San Martin Drive, Baltimore, MD 21218, USA

⁷ Crimean Astrophysical Observatory, P/O Nauchny Crimea 298409, Russia

⁸ School of Physics and Astronomy, Raymond and Beverly Sackler Faculty of Exact Sciences, Tel Aviv University, Tel Aviv 69978, Israel

⁹ Physics Department, Technion, Haifa 32000, Israel

¹⁰ Institute of Astronomy, School of Science, University of Tokyo, 2-21-1, Osawa, Mitaka, 181-0015 Tokyo, Japan

¹¹ McWilliam Center for Cosmology, Department of Physics, Carnegie Mellon University, 5000 Forbes Avenue, Pittsburgh, PA 15213, USA

¹² Department of Physics and Astronomy, Vanderbilt University, 6301 Stevenson Center, Nashville, TN 37235, USA

¹³ Department of Natural Sciences, The University of Michigan—Dearborn, 4901 Evergreen Road, Dearborn, MI 48128, USA

¹⁴ Department of Astronomy, University of Michigan, 500 Church Street, Ann Arbor, MI 48109, USA

¹⁵ Department of Physics and Astronomy, Dartmouth College, 6127 Wilder Laboratory, Hanover, NH 03755, USA

¹⁶ Department of Physics and Astronomy, Ohio University, Athens, OH 45701, USA

¹⁷ Department of Physical and Earth Sciences, Worcester State University, 486 Chandler Street, Worcester, MA 01602, USA

¹⁸ South Station of the Moscow MV, Lomonosov State University, Moscow, Russia, P/O Nauchny, 298409 Crimea, Russia

¹⁹ Center for AstroEngineering and Department of Electrical Engineering, Pontificia Universidad Católica de Chile,
 Av. Vicuña McKenna 4868, Santiago, Chile

²⁰ Department of Astrophysical Sciences, Princeton University, 4 Ivy Lane, Peyton Hall, Princeton, NJ 08544, USA

²¹ Warsaw University Observatory, Aleje Ujazdowskie 4, 00-478 Warszawa, Poland

Received 2014 July 20; accepted 2014 September 12; published 2014 October 23

ABSTRACT

A large reverberation-mapping study of the Seyfert 1 galaxy NGC 7469 has yielded emission-line lags for H β λ 4861 and He II λ 4686 and a central black hole mass measurement $M_{\text{BH}} \approx 1 \times 10^7 M_{\odot}$, consistent with previous measurements. A very low level of variability during the monitoring campaign precluded meeting our original goal of recovering velocity–delay maps from the data, but with the new H β measurement, NGC 7469 is no longer an outlier in the relationship between the size of the H β -emitting broad-line region and the luminosity of the active galactic nucleus. It was necessary to detrend the continuum and H β and He II λ 4686 line light curves and those from archival UV data for different time-series analysis methods to yield consistent results.

Key words: galaxies: active – galaxies: individual (NGC 7469) – galaxies: nuclei – galaxies: Seyfert

Online-only material: color figures, machine-readable tables

1. INTRODUCTION

Reverberation mapping (Blandford & McKee 1982; Peterson 1993, 2014) is a standard tool for probing the structure and kinematics of the broad-line region (BLR) in active galactic nuclei (AGNs). In its simplest form, the mean time delay between continuum and emission-line variations is measured, typically by cross-correlation of the respective light curves, and it is assumed that this represents the mean light-travel time across the BLR. By combining this with the emission-line width, which is assumed to reflect the velocity dispersion of gas whose motions are dominated by the mass of the central black hole, the black hole mass can be determined. Reverberation mapping in this form has been used to measure the black hole masses in

nearly 50 AGNs (for a recent compilation, see Bentz et al. 2013) to a typical accuracy of ~ 0.4 dex.

A decade ago, we undertook a consistent reanalysis of the reverberation-mapping database that existed at that time (Peterson et al. 2004). In the course of this work, we identified a number of cases where the BLR radius, mass estimates, or both would clearly benefit from improved monitoring. NGC 7469, one of Seyfert’s (1943) original galaxies distinguished by an abnormally bright core, is one such example.

The Seyfert 1 galaxy NGC 7469 was the subject of a large coordinated X-ray (Nandra et al. 1998, 2000), ultraviolet (UV; Wanders et al. 1997), and optical (Collier et al. 1998) monitoring campaign in 1996 June–July with the *Rossi X-Ray Timing Explorer*, the *International Ultraviolet Explorer (IUE)*, and several ground-based telescopes by the International AGN Watch consortium (Alloin et al. 1994). The program was supplemented with very high sampling-rate spectrophotometry

²² NSF Postdoctoral Research Fellow.

²³ Deceased, 2011 October 21.

²⁴ Hubble and Lyman Spitzer Fellow.

for 10 hr with the Faint Object Spectrograph on the *Hubble Space Telescope* to look for very short-timescale continuum variability (Welsh et al. 1998). This was the final year of *IUE* operations and an intensive reverberation-mapping program was intended to be part of a “Grand Finale.” One of the primary science goals of the *IUE* program was to recover a velocity–delay map (Horne et al. 2004) for the strong UV emission lines. The original target for the campaign was the Seyfert 1 galaxy Mrk 335, but an unfortunate gyroscope failure on *IUE* in 1996 March forced selection of an alternative target. NGC 7469 was deemed to be the most promising of a very small number of AGNs that would be accessible during the time period allocated for this program. Unfortunately, managing spacecraft pointing with *IUE* remained an issue that compromised the quality of the resulting data. The duration of the intensive part of the monitoring program was very limited and as a result, while reverberation lags were measured, it was not possible to obtain a reliable velocity–delay map from the *IUE* spectra.

The high-sampling rate UV/optical light curves did, however, reveal for the first time a statistically significant lag between continuum variations in the UV and those following at longer wavelengths (Wanders et al. 1997; Collier et al. 1998). The variations at 1825 Å, 4845 Å, and 6962 Å follow those at 1315 Å by $0.22^{+0.12}_{-0.13}$, $1.25^{+0.48}_{-0.35}$, and $1.84^{+0.93}_{-0.94}$ days, respectively (Peterson et al. 1998). Similar, but lower significance, interband continuum lags have also been seen in NGC 4151 (Peterson et al. 1998) and interband lags in the optical alone have been detected in 14 AGNs by Sergeev et al. (2005) at varying levels of significance. More recently, multiwavelength monitoring of NGC 2617, which recently underwent a dramatic change in “type” from Seyfert 1.8 to Seyfert 1, revealed that flux variations in all the continuum bands from the UV to NIR follow variations in the X-ray, with the lag increasing with wavelength. Moreover, the structure of the light curves becomes smoother with increasing wavelength, indicating some “time-smearing” associated with continuum reprocessing (Shappee et al. 2014).

Detection of interband lags is important, as it points to the mechanisms that cause continuum variability. There are also important implications for reverberation mapping. Specifically, it is necessarily assumed that the observable optical continuum is a reasonable proxy for the unobservable UV continuum that photoionizes the broad-line gas and drives the emission-line variations. A small time delay between the variations in the ionizing continuum and the optical continuum will result in a small underestimate of the BLR size. Even more important, however, is that if the optical continuum is a smoothed or time-smeared version of the ionizing continuum, there might be structure in the emission-line light curves that may not be present in the optical continuum light curves and recovery of the detailed structure of the BLR becomes more difficult.

The relationship between the continuum variations $\Delta C(t)$ and velocity-resolved emission-line variations $\Delta L(V, t)$ is usually expressed mathematically as

$$\Delta L(V, t) = \int_0^\infty \Psi(V, \tau) \Delta C(t - \tau) d\tau, \quad (1)$$

where $\Psi(V, \tau)$ is the “transfer function” (Blandford & McKee 1982), or velocity–delay map (Horne et al. 2004), which is the observed emission-line response to a delta-function continuum outburst. This simple linear formulation is justified by the fact that the continuum and emission-line variations are generally quite small (10%–20%) on reverberation timescales. The technical goal of a reverberation program is to recover the

velocity–delay map $\Psi(\Delta V, \tau)$ from the data and thus infer the geometry and kinematics of the BLR. However, if the optical continuum light curve is not a good surrogate for the variability of the ionizing continuum, then the fidelity with which we can recover velocity–delay maps is fundamentally limited. On the basis of the data obtained in the observing campaign described here, we suggest that this may be the case in NGC 7469.

Here we describe an optical reverberation-mapping monitoring program on NGC 7469 that was undertaken with the primary goal of obtaining a velocity–delay map for its H β λ 4861 and He II λ 4686 emission lines. We describe the observations and data analysis in Section 2. Our time-series analysis is presented in Section 3 and our black hole mass measurement is explained in Section 4. We briefly discuss and summarize our results in Section 5.

2. OBSERVATIONS AND DATA ANALYSIS

The data used in this study were obtained during a four month long observing campaign carried out in late 2010. The results for the other five objects observed in this campaign have been published by Grier et al. (2012b). We follow the data analysis procedures described in that study. When needed, we adopt a cosmological model with $\Omega_m = 0.3$, $\Omega_\Lambda = 0.70$, and $H_0 = 70 \text{ km s}^{-1} \text{ Mpc}^{-1}$.

2.1. Observations

We obtained 73 spectra with the Boller and Chivens CCD spectrograph on the MDM Observatory 1.3 m McGraw-Hill telescope on Kitt Peak. The data were collected over the course of 120 nights from 2010 August 31 to December 28. We used a 350 mm^{-1} grating to obtain a dispersion of $1.33 \text{ Å pixel}^{-1}$. We set the grating for a central wavelength of 5150 Å, which resulted in spectral coverage over the range of 4400–5850 Å. The slit was oriented north–south (position angle P.A. = 0°) with a projected width of $5''.0$ that produces a spectral resolution of 7.9 Å . We used an extraction window of $12''.0$ along the slit.

To supplement our spectra in estimating the driving continuum light curve, we obtained V-band imaging observations of NGC 7469 at several additional observatories. We obtained 74 images using the 70 cm telescope at the Crimean Astrophysical Observatory (CrAO) with the AP7p CCD, which has 512×512 pixels with a $15' \times 15'$ field of view when mounted at prime focus. We also obtained 66 epochs from the 46 cm Centurion telescope at Wise Observatory of Tel-Aviv University using an STL-6303E CCD with 3072×2048 pixels, with a field of view of $75' \times 50'$. Further V-band observations were obtained for seven epochs using the University of Tokyo’s 1.0 m miniTAO telescope stationed in Chile. We used the ANIR CCD camera (Motohara et al. 2008), which has a pixel scale of $0''.34 \text{ pixel}^{-1}$ and a field of view of $6' \times 6'$. Finally, we obtained observations of NGC 7469 for 56 epochs using the SMARTS CTIO 1.3 m telescope in Chile with the ANDICAM CCD camera, which has a field of view of $6' \times 6'$, 1024×1024 pixels, and a pixel scale of $0''.371 \text{ pixel}^{-1}$.

2.2. Data Processing and Light Curves

To place the reduced spectra on an absolute flux scale, we assume that the [O III] λ 5007 narrow-line flux is constant. Because of the relatively long light-travel time across the narrow-line region and because of the long recombination times, this is a good assumption on reverberation timescales, although narrow-line variability has been detected in other

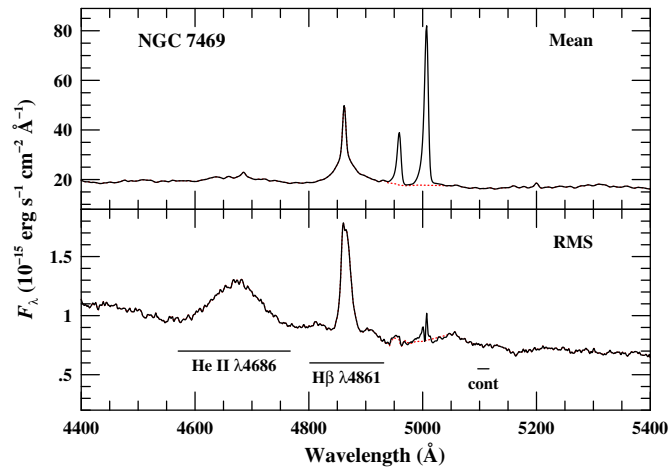


Figure 1. Rest-frame ($z = 0.01632$) mean (top panel) and RMS (bottom panel) spectra of NGC 7469. The dashed red lines show the spectra where the [O III] $\lambda\lambda 4959, 5007$ lines are removed prior to combining the individual spectra. The integration limits for He II $\lambda 4686$, H β $\lambda 4861$, and the continuum are indicated by horizontal lines in the bottom panel.

(A color version of this figure is available in the online journal.)

AGNs on timescales as short as years (e.g., Peterson et al. 2013). We used a reference spectrum created by averaging spectra taken on photometric nights and scale all of our spectra to match this reference spectrum. We measure the average [O III] $\lambda 5007$ flux in the reference spectrum to be $(6.14 \pm 0.12) \times 10^{-13} \text{ erg s}^{-1} \text{ cm}^{-2}$, which we adopt as the absolute flux for this object. This value is in general agreement with the [O III] $\lambda 5007$ flux reported by Collier et al. (1998). We then scaled each individual spectrum to the reference spectrum using a χ^2 goodness-of-fit estimator method to minimize the flux differences between the spectra (van Groningen & Wanders 1992). Figure 1 shows the mean and root mean square (RMS) residual spectra of NGC 7469 based on the calibrated MDM spectra. Emission-line light curves were created by fitting a linear continuum underneath the emission lines in each scaled spectrum and integrating the flux above them. The H β $\lambda 4861$ integrations were done between the observed-frame wavelengths of 4880–5012 Å, and the He II $\lambda 4686$ fluxes were measured between 4645–4845 Å. The 5100 Å continuum light curves were created by taking the average flux measured from 5180–5200 Å in the observed frame.

We produced light curves from our V-band photometry using the image subtraction software package ISIS (Alard & Lupton 1998; Alard 2000). We follow the procedures of Shappee & Stanek (2011), wherein the images are first aligned using the program Sexterp (Sivert et al. 2012) including its optional resampling utility `is3_interp`. We then follow the steps outlined by Alard, using ISIS to create a reference image for the field using the 20–30 images with the best seeing and lowest background counts. ISIS convolves the images with a spatially variable convolution kernel to transform all images to the same point-spread function (PSF) and background level. The resulting images are stacked using a 3σ rejection limit from the median. We then used ISIS to convolve the reference image to match each individual image in the data set and subtract each individual frame from the convolved reference image. We extract light curves for the nucleus of the galaxy from these subtracted images using ISIS to place a PSF-weighted aperture over the nucleus and measure the residual flux.

The spectroscopic continuum light curve was then merged with the photometric light curves to create our final continuum

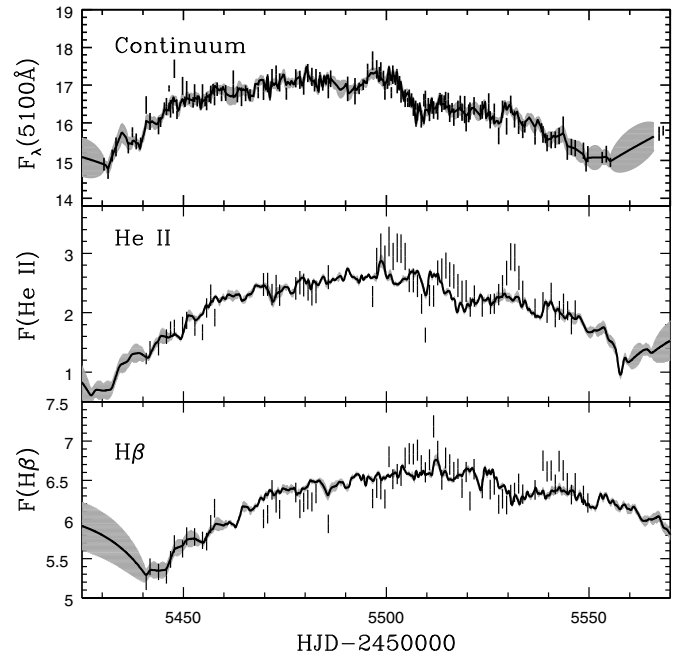


Figure 2. Combined light curves for NGC 7469, along with the JAVELIN models. The black vertical bars show the original data, and the solid black line shows the mean of the JAVELIN light curve models most consistent with the data. The gray shaded region shows the standard deviation of values about the mean. Continuum fluxes are in units of $10^{-15} \text{ erg s}^{-1} \text{ cm}^{-2} \text{ Å}^{-1}$ and emission-line fluxes are in units of $10^{-13} \text{ erg s}^{-1} \text{ cm}^{-2}$.

Table 1
Continuum Fluxes

HJD ^a	Observatory ^b	$F_{\text{cont}}(5100 \text{ Å})^c$
5430.430	C	14.90 ± 0.17
5430.780	S	14.88 ± 0.02
5431.420	C	14.66 ± 0.15
5432.410	C	15.13 ± 0.16
5433.370	C	15.36 ± 0.25
5436.390	C	15.34 ± 0.15
5437.340	W	15.43 ± 0.02
5437.400	C	15.75 ± 0.13
5437.790	S	15.53 ± 0.01
5438.360	C	15.51 ± 0.21
5438.390	W	15.46 ± 0.02
5438.810	S	15.46 ± 0.01

Notes.

^a Heliocentric Julian Date (−2450000).

^b Observatory code: C = CRAO, W = WISE, M = MDM, S = SMARTS, T = miniTAO.

^c Continuum fluxes are in units of $10^{-15} \text{ erg s}^{-1} \text{ cm}^{-2} \text{ Å}^{-1}$.

(This table is available in its entirety in a machine-readable form in the online journal. A portion is shown here for guidance regarding its form and content.)

light curve. To correct for the differences in host-galaxy starlight that enters the apertures, we applied a multiplicative scale factor as well as an additive flux adjustment to each photometric light curve (see Peterson et al. 1995). The merged continuum light curve and the MDM spectroscopic light curves for H β and He II are shown as the black vertical bars in Figure 2. The continuum light curve fluxes are given in Table 1, with each data point labeled according to the observatory at which it was obtained. The H β and He II fluxes from the MDM spectra are listed in Table 2. Final light curve statistics for all three light

Table 2
Emission-line Fluxes

HJD ^a	$F(\text{H}\beta)^b$	$F(\text{He II } \lambda 4686)^b$
5440.801	5.203 ± 0.102	1.228 ± 0.096
5441.763	5.398 ± 0.106	1.413 ± 0.111
5443.820	5.331 ± 0.104	1.391 ± 0.109
5445.779	5.286 ± 0.104	1.596 ± 0.125
5446.787	5.491 ± 0.108	1.719 ± 0.135
5447.767	5.688 ± 0.111	1.748 ± 0.137
5449.767	5.624 ± 0.110	1.790 ± 0.140
5450.758	5.788 ± 0.113	1.871 ± 0.147
5452.773	5.778 ± 0.113	1.751 ± 0.137
5454.698	5.734 ± 0.112	1.671 ± 0.131
5455.696	5.717 ± 0.112	2.080 ± 0.163
5456.744	5.943 ± 0.116	2.295 ± 0.180
5457.695	6.145 ± 0.120	1.918 ± 0.150

Notes.^a Heliocentric Julian Date (-2450000).^b Emission-line fluxes are in units of $10^{-13} \text{ erg s}^{-1} \text{ cm}^{-2}$.

(This table is available in its entirety in a machine-readable form in the online journal. A portion is shown here for guidance regarding its form and content.)

curves are given in Table 3. We also include the statistics for the AGN continuum only, with our best estimate of the starlight contamination ($F_{\text{gal}} = (8.7 \pm 0.9) \times 10^{-15} \text{ erg s}^{-1} \text{ cm}^{-2} \text{ \AA}^{-1}$; Bentz et al. 2013²⁵) subtracted from each of the continuum measurements that are given in Table 1. It is worth noting that the mean optical flux from the AGN alone during the AGN Watch program was $F_{\text{AGN}} = 5.14 \times 10^{-15} \text{ erg s}^{-1} \text{ cm}^{-2} \text{ \AA}^{-1}$ (Bentz et al. 2009); i.e., the AGN was $\sim 52\%$ more luminous in 2010 than it was in 1996.

3. TIME-SERIES ANALYSIS

Inspection of the light curves in Figure 2 and the variability statistics (Table 3) show that the overall levels of variability were of much lower amplitude than normally desirable for a reverberation experiment. Figure 3 shows a comparison of the fractional variation F_{var} observed over this campaign with 116 previous successful reverberation timeseries (Peterson et al. 2004). The continuum light curve lacks the strong short-timescale variations that produce the clearest reverberation signatures. This necessarily severely limits the amount of information that we can extract from these data. Also, we note that there are structures in the emission-line light curves that are not present in the continuum light curve. As mentioned in Section 1, this leads us to suspect that the far-UV ionizing continuum light curve has more short-timescale structure than the reprocessed optical continuum. The broad-line gas reprocesses the ionizing photons into emission-line photons rapidly (as the recombination time at BLR densities is less than an hour). The continuum reprocessing timescale, on the other hand, must be somewhat longer and thus slightly smears out the shorter-timescale variations in the shorter-wavelength continuum. We keep this in mind as we consider the response of the emission lines to the continuum variations.

We use two different methods to examine the time-delayed response of the $\text{H}\beta$ $\lambda 4861$ and $\text{He II } \lambda 4686$ emission lines to the continuum variations, as we describe below. We also attempted

to recover velocity–delay maps as we did for other sources observed in the same campaign (Grier et al. 2013b), but we were unsuccessful on account of the low level of variability in this source during the monitoring campaign.

3.1. Cross-correlation Analysis

For an initial attempt to determine the emission-line lags, we cross-correlated the continuum light curve (Table 1) with the emission-line light curves (Table 2). The methodology we use was first described by Gaskell & Sparke (1986) and Gaskell & Peterson (1987) and later significantly modified by White & Peterson (1994) and updated by Peterson et al. (1998, 2004). The cross-correlation functions (CCFs) are shown in the top panels of Figure 4, along with the continuum autocorrelation function. The cross-correlation results are given in the first two rows of Table 4, where τ_{peak} is the value of the time delay or lag where the CCF is maximized (r_{max}). The centroid of the CCF peak τ_{cent} is computed from all neighboring points near τ_{peak} with $r(\tau) \geq 0.8r_{\text{max}}$, although some experimentation shows that the centroid is insensitive to the threshold used in the computation. The quoted 1σ uncertainties were determined by using the model-independent Monte Carlo method of flux randomization and random subset sampling (FR/RSS) described by Peterson et al. (1998, 2004). The cross-correlation centroid distributions from this process are also shown in the middle panels of Figure 4.

The CCFs for both lines (Figure 4) have broad plateaus extending from ~ 10 days for $\text{H}\beta$ and from close to zero days for He II to much larger lags, leaving the correct lags uncertain, although the $\text{H}\beta$ lag is clearly longer than the four to five day lag from the 1996 campaign (Collier et al. 1998; Peterson et al. 2004). The FR/RSS centroid distribution functions shown in the middle panels of Figure 4 are less well defined than in most cases, and the He II centroid distribution function has a broad tail extending to nearly 20 days.

3.2. JAVELIN Analysis

Zu et al. (2011) have developed an alternative method of measuring reverberation time lags called Stochastic Process Estimation for AGN Reverberation (SPEAR), that was subsequently upgraded to the software package we used in our analysis, JAVELIN.²⁶ SPEAR and JAVELIN have been used successfully to determine time lags by Grier et al. (2012a, 2012b), and to model continuum light curve behavior (Grier et al. 2013b). As with cross-correlation, this method assumes all emission-line light curves are scaled and shifted versions of the continuum light curve. JAVELIN models the continuum as an autoregressive process using a damped random walk model, which has been demonstrated to be a good statistical model of AGN variability (e.g., Kelly et al. 2009; Kozłowski et al. 2010; MacLeod et al. 2010, 2012; Zu et al. 2013). The software explicitly builds a model of the light curve and transfer function and fits it to the data by maximizing the likelihood of the model. JAVELIN then computes uncertainties using the Bayesian Markov Chain Monte Carlo method.

We used JAVELIN to determine the time lag between the 5100 \AA continuum and both the $\text{H}\beta$ and He II emission lines. The JAVELIN results are also given in Table 4. The posterior distributions of the successful JAVELIN models are shown in the bottom panels of Figure 4. We see that the JAVELIN distributions are highly inconsistent with the FR/RSS distributions immediately above.

²⁵ The entry for the host-galaxy flux for NGC 7469 in Table 12 of Bentz et al. (2013) is in error. The correct value is used here.

²⁶ <http://www.astronomy.ohio-state.edu/~yingzu/codes.html#javelin>

Table 3
Light Curve Statistics

Time Series (1)	N (2)	Sampling Interval (days)		Mean ^a Flux (5)	Mean Fractional Error (6)	F_{var} (7)	R_{max} (8)
		$\langle T \rangle$ (3)	T_{median} (4)				
5100 Å	276	0.5	0.40	16.54 ± 0.60	0.007	0.035	1.20 ± 0.02
5100 Å, AGN only	276	0.5	0.40	7.84 ± 0.60	0.015	0.074	1.50 ± 0.06
H β λ 4861	73	1.5	1.00	6.31 ± 0.41	0.020	0.062	1.38 ± 0.04
He II λ 4686	73	1.5	1.00	2.29 ± 0.44	0.078	0.172	2.60 ± 0.29

Notes. Column 1 lists the spectral feature and Column 2 gives the number of points in the individual light curves. Columns 3 and 4 list the average and median time spacing between observations, respectively. Column 5 gives the mean flux of the feature in the observed frame and Column 6 shows the mean fractional error that is computed based on observations that are closely spaced in time. Column 7 gives the excess variance, defined by

$$F_{\text{var}} = \frac{\sqrt{\sigma^2 - \delta^2}}{\langle f \rangle}, \quad (3)$$

where σ^2 is the flux variance of the observations, δ^2 is the mean square uncertainty, and $\langle f \rangle$ is the mean observed flux. Column 8 is the ratio of the maximum to minimum flux in each light curve.

^a Continuum and emission-line fluxes are given in $10^{-15} \text{ erg s}^{-1} \text{ cm}^{-2} \text{ Å}^{-1}$ and $10^{-13} \text{ erg s}^{-1} \text{ cm}^{-2}$, respectively.

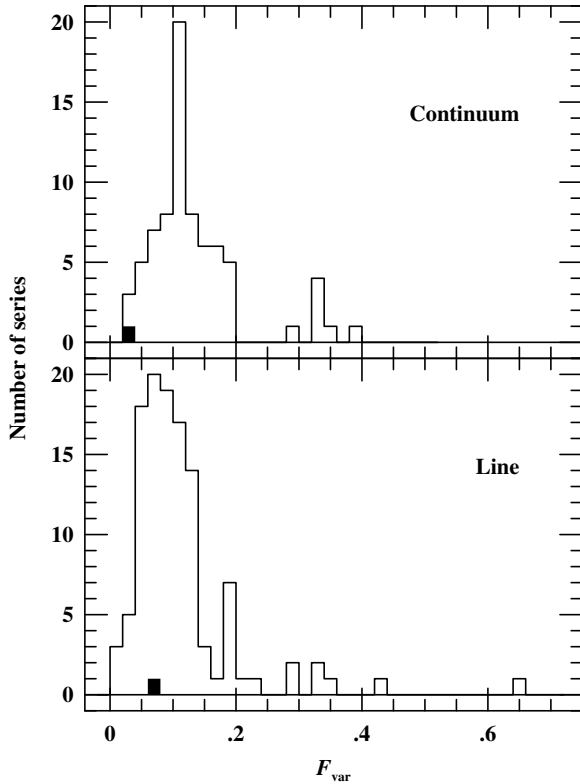


Figure 3. Distribution of fractional variability measures F_{var} for successful reverberation-mapping campaigns compiled by Peterson et al. (2004). The upper panel shows the continuum variations, usually in the optical and uncorrected for starlight contamination, and the lower panel shows line variations, usually for H β and uncorrected for narrow-line contamination. The values for the current campaign on NGC 7469, shown in black, indicate how comparatively little variability was detected in this campaign.

3.3. Analysis of Detrended Light Curves

When there is little short-timescale variability and much of the variability is on timescales comparable to the duration of the observing campaign, aliasing becomes an increasing problem.

The time delays measured by cross-correlation and with JAVELIN are much more inconsistent than we usually find in

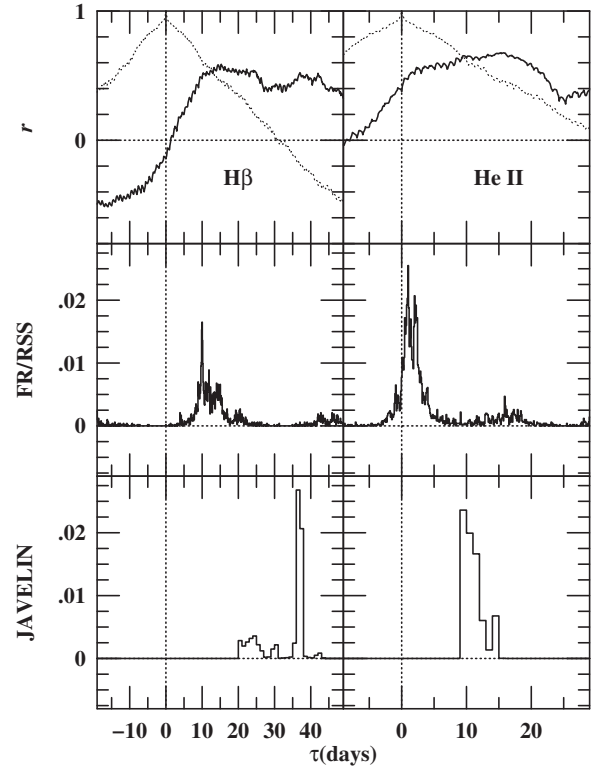


Figure 4. Time-series analysis results for H β (left column) and He II (right column), based on the light curves given in Tables 1 and 2 and shown in Figure 2. The top row shows the cross-correlation functions; the solid black lines show the CCFs for each emission line, and the gray dashed lines show the continuum autocorrelation function. The middle row shows the cross-correlation centroid distribution from 1000 FR/RSS realizations. The bottom row shows the posterior lag distributions from JAVELIN. The cross-correlation functions have no clearly defined maxima and the JAVELIN and cross-correlation results are in poor agreement.

reverberation studies, almost certainly as a consequence of the low amplitude of variability. Moreover, what little variability there is seems to be dominated by long-term quasi-parabolic trends where the light curves initially slowly rise, then fall. Trends longer than reverberation timescales can yield misleading reverberation results as shown by, e.g., Grier et al. (2008).

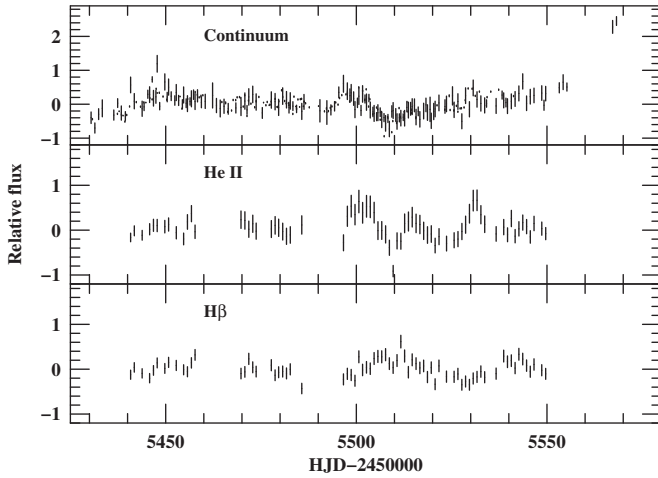


Figure 5. Continuum (top), He II (middle), and H β (bottom) light curves after detrending by subtracting a low-order polynomial from the original light curves shown in Figure 2.

Table 4
H β , He II λ 4686, and C IV Time-series Results^a

Parameter (1)	This Campaign		Archival
	H β (days) (2)	He II (days) (3)	C IV (days) (4)
Original:			
τ_{cent}	$11.8^{+4.2}_{-2.6}$	$1.9^{+7.5}_{-1.6}$	$2.6^{+0.3}_{-0.3}$
τ_{peak}	$11.8^{+4.2}_{-2.7}$	$2.0^{+7.4}_{-1.7}$	$2.5^{+0.5}_{-0.5}$
$\Delta\tau_{\text{cent}}(\text{H}\beta - \text{He II})$	$8.4^{+2.0}_{-2.0}$
τ_{JAVELIN}	$23.6^{+1.8}_{-2.7}$	$10.4^{+2.1}_{-0.7}$	$10.8^{+0.2}_{-0.2}$
Detrended:			
τ_{cent}	$10.9^{+3.5}_{-1.3}$	$1.3^{+0.9}_{-0.7}$	$2.3^{+0.3}_{-0.3}$
τ_{peak}	$11.2^{+3.3}_{-1.4}$	$1.2^{+1.1}_{-0.8}$	$2.2^{+0.5}_{-0.3}$
$\Delta\tau_{\text{cent}}(\text{H}\beta - \text{He II})$	$9.0^{+2.0}_{-1.5}$
τ_{JAVELIN}	$10.0^{+1.2}_{-0.4}$	$0.8^{+0.7}_{-0.2}$	$2.3^{+0.3}_{-0.2}$

Notes. ^a All time delays are given in the observed frame. The “original” C IV time delays are from Peterson et al. (2004) and Zu et al. (2011).

Welsh (1999) suggested that reverberation measurements based on cross-correlation analysis could be improved by “detrending” the light curves: when light curves are dominated by trends longer than the reverberation timescale, we fit the light curves with low-order polynomials, and subtract off these longer-term trends prior to applying the cross-correlation analysis. In previous experiments (Denney et al. 2010), we found that detrending led to marked improvement in the results.

In Figure 5, we show the light curves from Figure 2 after detrending. The cross-correlation results based on the detrended data are shown in the top panels of Figure 6 and listed in Table 4, and the cross-correlation centroid distributions are shown in the middle panels of Figure 6. The posterior lag distributions from JAVELIN are shown in the bottom panels of Figure 6. Clearly, the He II and H β lags are much better defined using the detrended light curves and there is consistency between the cross-correlation and JAVELIN results. Moreover, direct cross-correlation of the emission lines with each other yields lags that are statistically indistinguishable for the original and detrended data ($\Delta\tau_{\text{cent}}(\text{H}\beta - \text{He II})$ in Table 4).

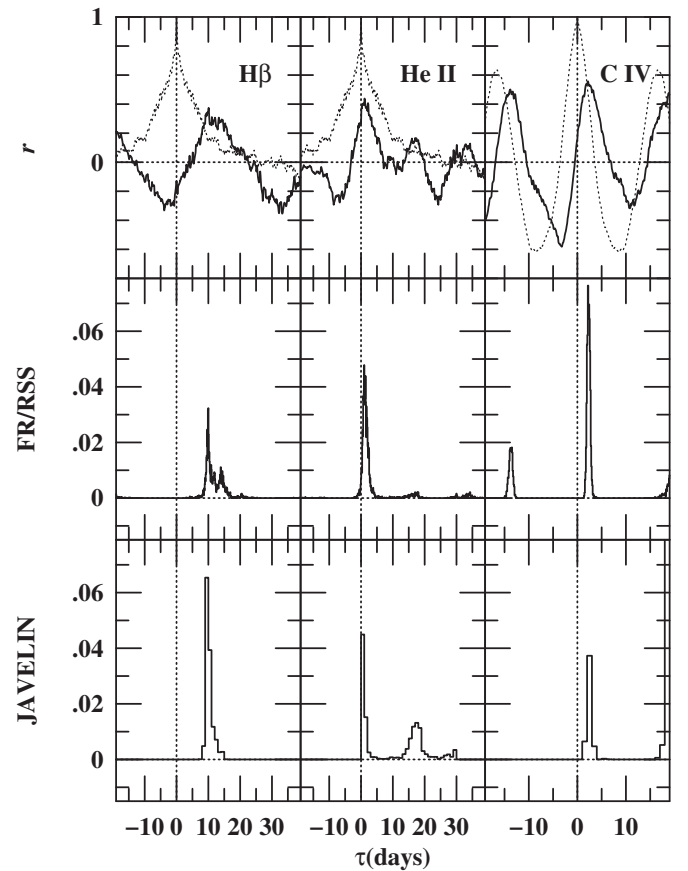


Figure 6. Time-series analysis results for H β (left column), and He II (middle column) based on the detrended light curves as shown in Figure 5 and for C IV λ 1549 (right column) based on archival *IUE* data. The top row shows the cross-correlation functions; the solid black lines show the CCFs for each emission line, and the gray dashed lines show the continuum autocorrelation function. The middle row shows the cross-correlation centroid distribution from 1000 FR/RSS realizations. The bottom row shows the lag distribution from JAVELIN. The results for H β and He II should be compared with those shown in Figure 4. The results for the detrended light curves are far more consistent.

The difference is also consistent with the difference between the two continuum–emission-line lags.

There was a similar discrepancy for the C IV λ 1549 emission line in the AGN Watch data on NGC 7469 (Zu et al. 2011). The lags for He II λ 1640 and Si IV λ 1400 were consistent, but in the case of the C IV λ 1549 line, the cross-correlation lag was measured to be ~ 2.5 days, while the JAVELIN time delay was nearly 11 days. We suspected that the C IV results might also be improved by detrending. This did indeed prove to be the case, as JAVELIN yields a C IV time delay that is in much better agreement with the cross-correlation result (Table 4 and Figure 6) after a simple linear detrending.

4. LINE WIDTH AND BLACK HOLE MASS CALCULATION

Assuming that the motion of the BLR gas is dominated by gravity and that radiation pressure can be neglected, the mass of the central black hole is given by

$$M_{\text{BH}} = f \left(\frac{c\tau\Delta V^2}{G} \right), \quad (2)$$

where τ is the emission-line time delay, ΔV is the velocity width, and f is a dimensionless factor that depends on the

Table 5
Emission-line Widths^a

Parameter	H β (km s ⁻¹)	He II (km s ⁻¹)	C IV (km s ⁻¹)
(1)	(2)	(3)	(4)
σ_{line} (mean)	1095 \pm 5	2306 \pm 8	1707 \pm 20
FWHM (mean)	4369 \pm 6	2197 \pm 339	1722 \pm 30
σ_{line} (RMS)	1274 \pm 126	2271 \pm 77	2619 \pm 118
FWHM (RMS)	1066 \pm 84	5607 \pm 315	4305 \pm 422

Notes. ^a Widths are in the rest frame of NGC 7469. C IV line widths are from Peterson et al. (2004) and Collin et al. (2006).

Table 6
Virial Products

Emission		Cross-correlation (FR/RSS)		JAVELIN	
Line	Reference	τ_{cent}	$M_{\text{vir}} (\times 10^6 M_{\odot})$	τ_{JAVELIN}	$M_{\text{vir}} (\times 10^6 M_{\odot})$
(1)	(2)	(3)	(4)	(5)	(6)
H β	1	10.8 ^{+3.4} _{-1.3}	3.41 ^{+1.27} _{-0.79}	9.8 ^{+1/2} _{-0.4}	3.11 ^{+0.73} _{-0.63}
He II λ 4686	1	1.3 ^{+0.9} _{-0.7}	1.30 ^{+0.93} _{-0.67}	0.8 ^{+0.7} _{-0.8}	0.86 ^{+0.76} _{-0.22}
C IV λ 1549	1,2,3	2.5 ^{+0.3} _{-0.2}	3.35 ^{+0.50} _{-0.40}	2.3 ^{+0.3} _{-0.3}	3.13 ^{+0.49} _{-0.39}
Si IV λ 1400	2,3	1.7 ^{+0.3} _{-0.3}	4.05 ^{+0.95} _{-0.95}	2.0 ^{+0.4} _{-0.5}	4.77 ^{+1.20} _{-1.40}
He II λ 1640	2,3	0.6 ^{+0.3} _{-0.4}	1.62 ^{+0.82} _{-1.09}	0.8 ^{+0.2} _{-0.2}	2.16 ^{+0.56} _{-0.56}
H β	3,4	4.5 ^{+0.7} _{-0.8}	1.90 ^{+0.61} _{-0.63}
H α	3,4	4.7 ^{+1.6} _{-1.3}	1.24 ^{+0.45} _{-0.37}
Weighted mean	2.22 \pm 0.24	...	2.46 \pm 0.26

References. (1) This work; (2) Wanders et al. 1997; (3) Peterson et al. 2004; (4) Collier et al. 1998.

structure, kinematics, and orientation of the BLR. The quantity in parentheses in Equation (2) contains just the observables and is sometimes referred to as the “virial product” M_{vir} (i.e., $M_{\text{BH}} = f M_{\text{vir}}$).

The BLR velocity dispersion can be characterized by either the FWHM or the line dispersion σ_{line} . To determine the best value of the line width and its uncertainty, we use Monte Carlo simulations similar to those used when determining the lag from the CCF. We run 200 simulations in which we create a mean and RMS spectrum from a randomly chosen subset of the spectra, obtaining a distribution of resolution-corrected line widths. We adopt the mean values of FWHM and σ_{line} from these simulations and adopt their standard deviation as our formal uncertainty. We measure σ_{line} and FWHM in both the mean and RMS spectra, and these appear in Table 5. There is some evidence that σ_{line} produces less biased mass measurements than FWHM (Peterson 2011), thus we prefer to use σ_{line} to compute M_{BH} . We also prefer to use measurements from the RMS spectrum, as this eliminates contamination from constant narrow line and other slowly varying components to isolate the broad emission components that are actually responding to the continuum variations. This prescription yields the virial products listed in Table 6.

A necessary condition for using reverberation results to estimate black hole masses is that the virial products for the various emission lines are the same. In Figure 7, we plot line width σ_{line} versus time delay for both τ_{cent} and τ_{JAVELIN} from the detrended light curves and find that the data are now generally quite consistent with the simple virial prediction.

All of our ignorance of the geometry, kinematics, and inclination of the BLR is subsumed in the scaling factor f that is needed to convert M_{vir} into M_{BH} . At the present time, it is difficult to

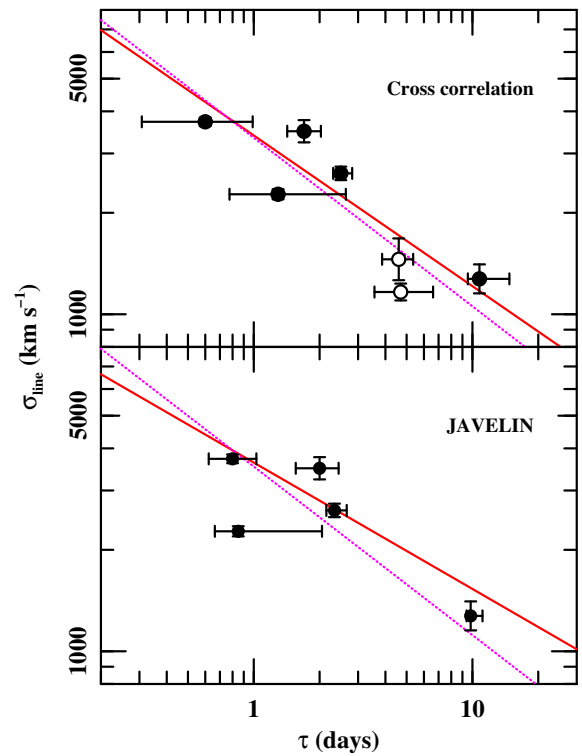


Figure 7. Relationship between emission-line width and lag. The top panel shows the relationship between line dispersion in the RMS spectrum and cross-correlation centroid τ_{cent} . The open circles are lower-confidence measurements of the H β and H α lines from the AGN Watch program in 1996. The red line is the fit to the relationship $\log \sigma_{\text{line}} = a + b \log \tau$, which has slope $b = -0.45 \pm 0.05$. The dotted magenta line is the best fit with a forced virial slope of $b = -0.5$. The bottom panel is exactly the same as the top panel, except that the time lags τ are from JAVELIN. The JAVELIN results for H α and H β from the AGN Watch program are ambiguous and therefore not included. The best-fit slope for these data is $b = -0.38 \pm 0.06$.

(A color version of this figure is available in the online journal.)

determine f for an individual source, although dynamical modeling of reverberation data is beginning to show great promise in this regard (Pancoast et al. 2012, 2014). In the absence of a determination of f for a specific source such as NGC 7469, we can determine an ensemble average value $\langle f \rangle$ by employing a secondary method to estimate AGN black hole masses. The commonly used method is to assume that the relationship between central black hole mass and host-galaxy bulge velocity dispersion, the $M_{\text{BH}}-\sigma_*$ relationship, is the same in active and quiescent galaxies (Onken et al. 2004). The most recent determination of the scale factor for reverberation-mapped AGNs is $\langle f \rangle = 4.31 \pm 1.05$ (Grier et al. 2013a). This estimate is consistent with recent results by Woo et al. (2010) and Park et al. (2012), who obtain estimates of $\langle f \rangle = 5.2$ and $\langle f \rangle = 5.1$, respectively, but it is about a factor of two larger than the value of $\langle f \rangle$ computed by Graham et al. (2011). Park et al. (2012) attribute this factor of two difference in $\langle f \rangle$ estimates to sample selection and to the regression method used for the calculations.

We estimate the mass of the black hole in NGC 7469 by using the weighted mean virial products in Table 6 and by taking $f = 4.31$ (Grier et al. 2013a). This yields masses of $9.57 (\pm 1.03) \times 10^6 M_{\odot}$ for the cross-correlation based results and $10.6 (\pm 1.12) \times 10^6 M_{\odot}$ for the JAVELIN measurements. The formal errors quoted here are the random components only, from the uncertainties on the lag and line width. The systematic error, estimated from the scatter around the $M_{\text{BH}}-\sigma_*$ relationship, is probably ~ 0.43 dex (Woo et al. 2010).

5. DISCUSSION AND SUMMARY

As we noted in Section 1, the earlier reverberation data on NGC 7469 were not especially good because the signal to noise of the UV data was suboptimal and the temporal sampling of the optical data was rather poor. Consequently, it was not too surprising that NGC 7469 was a significant outlier in the otherwise fairly tight relationship between AGN luminosity and $H\beta$ lag (Bentz et al. 2009), the AGN BLR “radius–luminosity relation.” The new $H\beta$ measurement places NGC 7469 within the scatter of this relationship.

We noted earlier that there are features in the emission-line light curves that are seen clearly in the emission-line light curves, but not in the continuum light curve. Specifically, these can best be seen in the detrended $He II$ light curve around HJD 2455515 and HJD 2455530 and the detrended $H\beta$ light curve around HJD 2455540 in Figure 5. We speculated that this might be a consequence of some sort of smoothing or re-processing of the ionizing continuum that occurs on timescales longer than the light-travel time between the locations where the ionizing and optical continua are produced. As an experiment, we used the general methodology of JAVELIN to model the observed line and continuum light curves as differently lagged and smoothed versions of an unobserved underlying UV continuum. These experiments were not successful. Either it is possible for short-timescale fluctuations to modify the line fluxes without affecting the continuum or some of the short-timescale structure in the line light curves is due to an unappreciated systematic error in their construction.

In summary, on account of the low level of variability in this campaign, we were unable to meet our primary goal of recovering velocity–delay maps for $H\beta$ and $He II$, as we did for other AGNs observed in the same campaign (Grier et al. 2013b), despite the intensive observational coverage. We were, however, able to recover emission-line lags for these two lines, but only after detrending the light curves. We also applied detrending to the UV continuum and $C IV \lambda 1549$ light curves from Wanders et al. (1997) and thus resolved the discrepancy between the $C IV$ lags measured by cross-correlation and JAVELIN analyses of (Zu et al. 2011). From these data, we were able to derive a black hole mass of $\sim 1 \times 10^7 M_\odot$ for the central black hole, using the most recent calibration of the reverberation mass scale (Grier et al. 2013a).

B.M.P., C.J.G., G.D.R., and R.W.P. are grateful for the support of the National Science Foundation through grant AST-1008882 to Ohio State University. M.C.B. gratefully acknowledges support from the NSF through CAREER grant AST-1253702. K.D.D. acknowledges support by the NSF through award AST-1302093 and from the Marie Curie Actions of the European Union’s Seventh Framework Programme FP7/2007-2013/ under REA grant agreement No. 300553. B.J.S., C.B.H., and J.L.V. acknowledge support by NSF Fellowships. C.S.K., A.M.M., and D.M.S. acknowledge the support of NSF grants AST-1004756 and AST-1009756. S.K. is supported at the Technion by the Kitzman Fellowship and by a grant from the Israel–Niedersachsen collaboration program. S.R. is supported at Technion by the Zeff Fellowship. S.G.S. acknowledges the support to CrAO in the frame of the “CosmoMicroPhysics” Target Scientific Research Complex Programme of the National Academy of Sciences of Ukraine (2007-2012). V.T.D. acknowledges the support of the Russian Foundation of Research (RFBR, project No. 12-02-01237-a). The CrAO CCD cameras were purchased through the US Civilian Research and

Development for Independent States of the Former Soviet Union (CRDF) awards UP1-2116 and UP1-2549-CR-03. This research has been partly supported by the Grants-in-Aid of Scientific Research (17104002, 20041003, 21018003, 21018005, 22253002, and 22540247) of the Ministry of Education, Science, Culture and Sports of Japan. This research has made use of the NASA/IPAC Extragalactic Database (NED), which is operated by the Jet Propulsion Laboratory, California Institute of Technology, under contract with the National Aeronautics and Space Administration.

REFERENCES

- Alard, C. 2000, *A&AS*, **144**, 363
 Alard, C., & Lupton, R. H. 1998, *ApJ*, **503**, 325
 Alloin, D., Clavel, J., Peterson, B. M., Reichert, G. A., & Stirpe, G. M. 1994, in *Frontiers of Space and Ground-based Astronomy*, ed. W. Wamsteker, M. S. Longair, & Y. Kondo (Dordrecht: Kluwer), 423
 Bentz, M. C., Peterson, B. M., Netzer, H., Pogge, R. W., & Vestergaard, M. 2009, *ApJ*, **697**, 160
 Bentz, M. C., Peterson, B. M., Netzer, H., Pogge, R. W., & Vestergaard, M. 2013, *ApJ*, **767**, 149
 Blandford, R. D., & McKee, C. F. 1982, *ApJ*, **255**, 419
 Collier, S. J., Horne, K., Kaspi, S., et al. 1998, *ApJ*, **500**, 162
 Collin, S., Kawaguchi, T., Peterson, B. M., & Vestergaard, M. 2006, *A&A*, **456**, 75
 Denney, K. D., Peterson, B. M., Pogge, R. W., et al. 2010, *ApJ*, **721**, 715
 Gaskell, C. M., & Peterson, B. M. 1987, *ApJS*, **65**, 1
 Gaskell, C. M., & Sparke, L. S. 1986, *ApJ*, **305**, 175
 Graham, A. W., Onken, C. A., Athanassoula, E., & Combes, F. 2011, *MNRAS*, **412**, 2211
 Grier, C. J., Martini, P., Watson, L. C., et al. 2013a, *ApJ*, **773**, 90
 Grier, C. J., Peterson, B. M., Bentz, M. C., et al. 2008, *ApJ*, **688**, 837
 Grier, C. J., Peterson, B. M., Horne, K., et al. 2013b, *ApJ*, **764**, 47
 Grier, C. J., Peterson, B. M., Pogge, R. W., et al. 2012a, *ApJ*, **744**, L4
 Grier, C. J., Peterson, B. M., Pogge, R. W., et al. 2012b, *ApJ*, **755**, 60
 Horne, K., Peterson, B. M., Collier, S. J., & Netzer, H. 2004, *PASP*, **116**, 465
 Kelly, B. C., Bechtold, J., & Siemiginowska, A. 2009, *ApJ*, **698**, 895
 Kozłowski, S., Kochanek, C. S., Udalski, A., et al. 2010, *ApJ*, **708**, 927
 MacLeod, C. L., Ivezić, Ž., Kochanek, C. S., et al. 2010, *ApJ*, **721**, 1014
 MacLeod, C. L., Ivezić, Ž., Sesar, B., et al. 2012, *ApJ*, **753**, 106
 Motohara, K., Mitani, N., Sako, S., et al. 2008, *Proc. SPIE*, **7014**, 70142
 Nandra, K., Clavel, J., Edelson, R. A., et al. 1998, *ApJ*, **505**, 594
 Nandra, K., Le, T., George, I. M., et al. 2000, *ApJ*, **544**, 734
 Onken, C. A., Ferrarese, L., Merritt, D., et al. 2004, *ApJ*, **615**, 645
 Pancoast, A., Brewer, B. J., Treu, T., et al. 2012, *ApJ*, **754**, 49
 Pancoast, A., Brewer, B. J., Treu, T., et al. 2014, *MNRAS*, in press (arXiv:1311.6475)
 Park, D., Kelly, B. C., Woo, J.-H., & Treu, T. 2012, *ApJS*, **203**, 6
 Peterson, B. M. 1993, *PASP*, **105**, 247
 Peterson, B. M. 2011, in *Proceedings of Science, POS(NLS1)034*, Narrow-line Seyfert 1 Galaxies and Their Place in the Universe, ed. L. Foschini et al. (Trieste: PoS), 32
 Peterson, B. M. 2014, *SSRv*, **183**, 253
 Peterson, B. M., Denney, K. D., De Rosa, G., et al. 2013, *ApJ*, **779**, 109
 Peterson, B. M., Ferrarese, L., Gilbert, K. M., et al. 2004, *ApJ*, **613**, 682
 Peterson, B. M., Pogge, R. W., Wanders, I., Smith, S. M., & Romanishin, W. 1995, *PASP*, **107**, 579
 Peterson, B. M., Wanders, I., Horne, K., et al. 1998, *PASP*, **110**, 660
 Sergeev, S. G., Doroshenko, V. T., Golubinskiy, Yu. V., Merkulova, N. I., & Sergeeva, E. A. 2005, *ApJ*, **622**, 129
 Seyfert, C. K. 1943, *ApJ*, **97**, 28
 Shappee, B. J., Prieto, J. L., Grupe, D., et al. 2014, *ApJ*, **788**, 48
 Shappee, B. J., & Stanek, K. Z. 2011, *ApJ*, **733**, 124
 Siverd, R. J., Beatty, T. G., Pepper, J., et al. 2012, *ApJ*, **761**, 123
 van Groningen, E., & Wanders, I. 1992, *PASP*, **104**, 700
 Wanders, I., Peterson, B. M., Alloin, D., et al. 1997, *ApJS*, **113**, 69
 Welsh, W. F. 1999, *PASP*, **111**, 1347
 Welsh, W. F., Peterson, B. M., Koratkar, A. P., & Korista, K. T. 1998, *ApJ*, **509**, 118
 White, R. J., & Peterson, B. M. 1994, *PASP*, **106**, 879
 Woo, J.-H., Treu, T., Barth, A. J., et al. 2010, *ApJ*, **716**, 269
 Zu, Y., Kochanek, C. S., Kozłowski, S., & Udalski, A. 2013, *ApJ*, **765**, 106
 Zu, Y., Kochanek, C. S., & Peterson, B. M. 2011, *ApJ*, **735**, 80